

Seismic wave simulation in the presence of real volcano topography

Ripperger, J. ^{a,*} Igel, H. ^a Wassermann, J. ^b

^a*Department für Erd- und Umweltwissenschaften ,
Ludwig-Maximilians-Universität, Munich, Germany*

^b*Institut für Geowissenschaften, Universität Potsdam, Germany*

Abstract

We use a finite-difference method on a 3D-staggered grid to simulate seismic wave propagation in the presence of strong topography variations. An application to Merapi volcano, Indonesia is presented. In order to focus on the effect of topography on the seismic wave field, calculations are performed for a rather simple model with an isotropic point source and a homogeneous subsurface medium. Despite this simplicity of the model a complex wave field evolves. Results of the computation are shown in synthetic seismograms, snapshots of the wave field and in a particle motion analysis. Waves reflected and converted at the free surface can be identified. The first P-wave arrivals show linear polarization whereas at later times the wave field is a superposition of shear and Rayleigh waves resulting in a more complicated particle motion pattern. The effect of volcano topography on seismic waves can be clearly demonstrated. We confirm, that the finite-difference method we use is apt for numerical modeling in volcano seismology.

Key words: finite-difference, Merapi volcano, topography, particle motion, volcano seismology

1 Introduction

The main goal of volcano seismology is to extract information on the structure, the internal dynamics and the state of activity of a volcano from the seismic waves generated by its interior processes. One main difference to normal earthquake seismology is the wide variety of processes that can possibly

* Corresponding author. Presently at ETH Zurich, Switzerland
Email address: ripp@seismo.ifg.ethz.ch (Ripperger, J.).

act as sources of seismic waves. In addition, these sources are often located rather shallow and close to the receiver sites. Thus a far-field assumption will not hold and near-field effects of the source can play a major role. Finally, the wave field can be distorted by a complex internal structure of the volcanic edifice. However, the most pronounced interface encountered by seismic waves is provided by the free surface topography of the volcano. The main interest of this study is to analyze its influence on the seismic wave field by numerical forward modeling.

A variety of numerical methods have been proposed which account for free surface topography. Earlier studies focus on the effect of basic 2D-topography structures like ramps, trenches or ridges on top of an elastic half space (e.g. Fuyuki and Matsumoto, 1980; Kawase, 1988; Jih et al., 1988; Tessmer et al., 1992; Benites and Aki, 1994). Some more recently developed methods also deal with viscoelastic wave modeling in the presence of 2D-topographies (e.g. Robertsson and Holliger, 1997; Moczo et al., 1997; Ruud and Hestholm, 2001). An increasing number of authors treat the problem of 3D-topographies. The effects of fundamental shapes like cavities or hills are investigated for example by Sánchez-Sesma and Campillo (1991), Tessmer and Kosloff (1994), Bouchon et al. (1996), Ohminato and Chouet (1997) and Luzón et al. (1997). Some authors also study real 3D-topography cases (e.g. Frankel and Leith, 1992; Pitarka and Irikura, 1996; Hestholm, 1999). However, the previously mentioned studies are not directly investigating the situation in volcano seismology, but rather deal with the general influence of free surface topography. Only recently, studies focused explicitly on modeling seismic waves in the presence of a volcanic topography. Neuberg and Pointer (2000) present a detailed parameter study with a 2D-boundary element method and an application to the real topography of Montserrat. Almendros et al. (2001a,b) apply a finite-difference method to the real topography of Kilauea volcano, Hawaii. They perform the simulations to derive a synthetic slowness vector model which is used for an improved localization procedure.

In our present study we also use a finite-difference method. It is based on the work of Ohminato and Chouet (1997) like the one used by Almendros et al. (2001a,b). We want to take a closer look at the properties of the wave field influenced by volcano topography. Thus we apply the method to a homogeneous medium bounded by the real topography of Mount Merapi, Indonesia. Nevertheless, our long-term goal is to study the superposition of scattering due to topography *and* medium heterogeneities. This motivates our choice of a finite-difference method instead of a boundary element approach.

2 Numerical Simulations

2.1 Method

We use a finite-difference (FD) scheme to simulate seismic wave propagation. The implementation of free surface topography is realized by closely following the ideas of Ohminato and Chouet (1997). In their work the method is described in detail, therefore only a brief outline and the modifications we applied are presented here.

The method makes use of the displacement-stress formulation of the elastic wave equation on a staggered grid. The basic idea is to set the Lamé parameters λ and μ of the medium to zero above and directly at the free surface. Hereby also the stress values are set to zero at the respective grid points. The important point is to discretize the free surface only along certain planes of the numerical FD grid. This is done in a way that the shear stresses σ_{xy} are only exposed to the surface at a vertical edge or a vertical plane. Setting these stresses to zero at the free surface is physically correct. The shear stresses σ_{xz} and σ_{yz} only appear on horizontal edges or horizontal planes, ensuring that setting these to zero at the free surface is also correct. All the normal stresses are embedded inside the medium. They are treated explicitly by making use of the antisymmetry of normal stress across the free surface boundary. This specific discretization is described by Ohminato and Chouet (1997) as 'stacking unit material cells'.

The method was originally formulated (Ohminato and Chouet, 1997) for a standard two-point finite difference operator (e.g. Virieux, 1986). In our work we extend the algorithm inside the medium to higher accuracy by using a four-point FD operator (e.g. Graves, 1996) for the spatial partial derivatives. At the free surface boundary the spatial partial derivatives remain formulated by a two-point FD operator.

To avoid artificial reflections from the bottom and the sides of the simulation domain, Ohminato and Chouet (1997) suggest to use the absorbing boundary conditions of Clayton and Engquist (1977). As this condition did not produce sufficient results in our tests we add a damping region around the domain instead. Inside this 50 grid point wide damping region the amplitudes of the simulation values (i.e. stresses and displacements) are multiplied at each time step by factors decreasing from 1 at the beginning of the damping region to about 0.9 at the outermost grid point.

The source we use in our study is an isotropic point source. It is introduced via the three normal stress components, which are defined at the same grid

point in the center of the unit material cell.

The three component synthetic seismograms are also taken at one common grid point for each desired receiver position. Therefore the values of the displacements, which are defined at the faces of the unit material cell are interpolated to the midpoint of the respective cell.

2.2 Parameters

We present an application of this method to the real topography of Mount Merapi, Indonesia. The elevation model we use consists of 400×400 points with a grid spacing of $dx = dy = 15m$, thus covering an area of $6 \times 6km$ centered around the summit. In the model the summit has a height of $2970m$ above sea level and the simulating region extends to a depth of $1500m$ below sea level. Together with the 50 grid cell wide damping region on the sides and the bottom this leads to a final model size of $500 \times 500 \times 350$ points and a memory requirement of roughly $9.5GB$. The algorithm was coded for parallel computers by making use of the Message Passing Interface (MPI). In the present simulation the computation was distributed over 32 processors of the parallel supercomputer Hitachi SR8000 at the Leibniz-Rechenzentrum in Munich. The total simulation time was set to $8s$, resulting in 3049 time steps of $dt = 0.00262s$. The computation time summed up to about 13 hours.

The source is positioned $500m$ vertically below the summit. We obtained synthetic three-component velocity seismograms along a profile across the summit in EW-direction. In addition, we calculated seismograms for sites, where the seismometers of a network of small aperture arrays are positioned in reality (Wassermann and Ohrnberger, 2001). Figure 1 sketches an overview of the model setup without the damping region. Snapshots of the elastic wave field at the surface and along a vertical cross section have been calculated to improve the understanding of its evolution. All simulation and model parameters are listed in Table 1.

3 Results

3.1 Seismograms

The seismograms of the receivers along the profile are shown in Figure 2 together with their distribution along the topography. The dashed horizontal

line marks the starting time of the simulation. In this plot the amplitudes of each receiver are scaled by its hypocentral distance. On the EW-component the first P-wave onset is the most prominent feature, except for the central receivers. The first P-wave is followed by several converted and reflected phases. In general, it can be seen that the wave field on the smoother western flank of the volcano is different from that observed on the eastern flank with its more rugged terrain. Note for example the amplification for the receiver on the crest of the ridge on the right.

For a plane surface with an explosive source and a homogeneous model, nothing should be observed on the NS-component. But in fact, there are several distinct phases visible on this component. These phases are resulting only from the presence of the topography. On the vertical component, the first P-wave is the most prominent feature for the central receivers. For the receivers located more outwards to the west, the highest amplitudes appear for a later phase with high coherency between neighboring receivers. It is most likely a surface wave. This coherent wave is not observed on the eastern flank. This again constitutes an effect of the differently shaped reliefs on both slopes.

The seismograms for single stations of the arrays SUMM, KLT, GRW and KEN are plotted in Figures 3, 4,5 and 6 respectively. For all four Figures the amplitude scale is the same, but again the traces are scaled with the hypocentral distance of the respective receivers. The positive radial component is defined as pointing outward away from the source and the transverse component is defined positive to the left, when looking in the positive radial direction. The vertical component is labeled positive upwards.

At the array SUMM, which is located very close to the summit, most of the seismic energy is concentrated in the first second of the traces. Because of the short travel path, no separation into distinguishable P- SV- and surface waves has occurred. The transverse component shows very little energy.

The arrays KLT and GRW are located further away from the source than SUMM. They have about the same epicentral distance but different azimuths. Nevertheless their seismograms show the same basic patterns. The peak amplitude appears for the first onset of the radial component. The transverse component shows a significant amount of energy. The last array KEN is the one with the greatest epicentral distance. The P-wave amplitude is no longer dominating, but has about the same value as the surface wave amplitude. There is a distinct surface wave train visible on all three components, starting at about 3s.

3.2 Snapshots

In Figures 7 and 8 we show snapshots of the wave field at the free surface for different time steps. The velocity wave field has been split up in the dilatational and the rotational part by calculating its divergence and curl, respectively. Of the curl only the y-component is displayed, representing the rotational movements parallel to the x- and z-axis. Snapshots for the vertical cross section below the receiver profile are displayed in Figure 9.

The P-waves can be observed only on the snapshots of the divergence. For the times $t = 0.4s$ and $t = 0.8s$ of Figure 7 the P-waves can be seen propagating radially outward, retaining an almost circular shape. However, on the divergence snapshot for $t = 1.2s$ in Figure 7 the first one seems to be diffracted by the prominent ridge in the front part of the model. On the divergence snapshots of $t = 0.8, 1.2$ and $1.6s$ in Figure 9 the first P-wave can be seen clearly traveling downward with a undisturbed half-circular shape. The later phases in these snapshots are all P-waves reflected from the free surface. For these phases a clear focusing effect of the topography below the summit can be observed.

The same focusing is apparent for the shear waves from P-SV conversions at the free surface. These S-waves are visible on the snapshots of the curl in Figure 9 as a complex pattern of red and blue patches propagating downward with shear-wave velocity.

By the shallow explosive source a great amount of surface waves is generated. As these have a dilatational and a rotational part, they are both visible on the divergence and the curl snapshots. As can be seen in Figures 7 and 8 these surface waves show a very complex and heterogeneous pattern. Strong azimuthal amplitude variations can be observed. In addition, a local amplification at topographic structures is evident, e.g. in the curl snapshots for $t = 2.4s$ and $t = 2.8s$ of Figure 8.

3.3 Seismic Energy

The receiver profile is running directly above the source in EW-direction. Since we use an explosive source, no seismic energy would be present on the transverse (NS) component of these receivers if a flat surface would be bounding the homogeneous half-space. But we observe strong onsets on this component as well, especially for increasing epicentral distance. As a measure of the seismic energy present on one component of a receiver, we sum up the squared amplitudes of the velocity seismograms over the whole trace length. In Figure 10 we plot the energy of the transverse component and the total energy as

the sum over all three components. The total energy recorded at the receivers is decaying with epicentral distance. On the western part of the profile the decay is rather uniform and smooth. On the eastern part we observe a significantly different behavior. The values drop more rapidly at smaller epicentral distances and show two local peaks further outwards. These peaks appear to be correlated with topographic structures, indicating local amplification of the ground motion. The maximum energy of the transverse component is recorded closest to the summit. But the maximum of the ratio between the transverse and the total energy is located on the eastern flank, where it reaches values of up to 26%. Since all the energy on the transverse component results from the presence of the topography, this ratio provides a rough estimate for the contribution of topographic scattering to the total wave field.

3.4 Polarization

In the following we take a closer look at the polarization pattern of some selected receivers. In Figures 11 to 14 the particle motions of the central station of each sub-array are plotted for different time windows. We obtain the displacements by integrating in time over the velocity seismograms. Two projections of the motion are displayed, one into the XY-plane and the other into a vertical plane containing both receiver and source. The radial, transverse and vertical component are defined as above and are labeled in the figures as R, T and Z respectively. The amplitudes are given in arbitrary units, normalized to the maximum of all three components for each receiver.

Since the station SUMM is located very close to the source, its particle motion pattern (Fig. 11) is dominated by the linearly polarized first P-wave arrival, visible in the first time interval. In the second time window, a more or less elliptical motion in the RZ-plane can be observed with almost no transverse motion present at the same time. This points to a Rayleigh wave generated at the free surface close to the summit. However, its amplitude is still small compared to the P-wave.

At the site of the array GRW the arrival of the first P-wave with linear polarization in the radial direction is also clearly visible (Fig. 12). In the following time intervals we observe two retrograde elliptical movements in the RZ-plane separated by a sharp bend in the particle trajectory. This most probably represents two subsequent arrivals of surface waves. However, at the same time the particle motion is not confined to the RZ-plane, but there is also a significant transverse motion present.

In the first time window of KLT (Fig. 13) the arrivals of the direct and the reflected P-wave can be observed as two distinct linearly polarized impulses separated by a jerk in the trajectory. They are followed by a sequence of strong transverse and vertical motion without a significant radial content. This may

represent S-waves from conversions at the free surface. In the third time interval a retrograde, almost circular movement appears in the RZ-plane, while still some transverse movement is present.

The array KEN is located at the greatest distance from the source. Due to this longer travel paths, some later phases can be separated more clearly (Fig. 14). The first P-wave arrival is linearly polarized, but is rotated about 7-8 degrees in the negative transverse direction, i.e. to the south in this case. Still in the first time window, the arrival of another linearly polarized wave can be observed. It is rotated another 7-8 degrees to the south and most probably marks the reflected P-wave. In the second and third time interval we can again observe the superposition of multiple phases of shear and surface waves. Remarkably about this receiver location is the presence of two phases linearly polarized in the horizontal plane in the fourth and fifth time window. Their origin is not completely clear. As their polarization direction is more or less aligned with the steep valleys and ridges in the vicinity of the receiver, they may result from energy trapped inside and traveling along these ridges.

The particle motions at the receivers along the profile are plotted in Figures 15 and 16. Here, the projection of the particle trajectories are given in the XY- and the XZ-plane respectively. As the profile is aligned along the X-axis above the source, the X-component is identical with the radial component and the Y-component is equal to the transverse component. Only the sign of the transverse component would be the opposite for receiver locations on the negative X-axis. Except for the linear polarization of the first P-wave arrival for almost all receivers, the particle motions show a very heterogeneous pattern. No continuous trend of certain polarization properties can be traced along the profile. In addition, we observe a significant difference between the behavior on the eastern and the western flank of the volcano.

4 Discussion

Our motivation was to demonstrate and to analyze the effect of topography in volcano seismology by numerical forward modeling. Doing this, it is always necessary to be aware of the assumptions and simplifications made in creating the model and also to have a look on the limitations of the numerical method.

One major problem of the finite-difference method we used here is the block-like representation of topography. Artefacts from the steps of the numerical grid have been reported (Moczo et al., 1997). We were also able to observe such artificial diffractions during the testing phase of our algorithm. However, these effects subside with increasing grid refinement. Ohminato and Chouet

(1997) suggest a ratio of 25 grid points per smallest wavelength, which they define as $\lambda_{min} = \frac{v_s}{2f_0}$ with the S-wave velocity v_s and the dominant source frequency f_0 . The results of our tests confirm this condition to be absolutely necessary to suppress unwanted diffractions (Ripperger, 2001). As this condition is met in our simulation, we consider the evolving wave pattern with its multiple diffractions, reflections and conversions as due to real physical effects.

However, the requirement of very fine grid spacing puts a serious limit on the frequency range, that can be investigated. In our case, we are able to use a dominant source frequency of $2Hz$. Nevertheless, some general effects can be observed in our simulation. A complex, heterogeneous wave field is emerging due to the presence of the rather steep and rugged free surface topography of the volcano. Strong surface waves are generated and dominate the wave field at later times. These surface waves do not show simple Rayleigh wave characteristics. There is also a strong SH-wave motion present.

5 Conclusion and Outlook

We conclude that the finite-difference method we use is a convenient method to simulate elastic wave propagation in the presence of free surface topography and is numerically stable even for strong topography variations as encountered in a volcanic setting. An important drawback is the requirement of a very fine grid spacing to avoid unwanted artefacts.

The influence of free surface topography on the seismic wave field can be clearly demonstrated. Future studies are planned to compare it with the effect of medium heterogeneities and different source types and locations.

In general, numerical modeling has proven to be an interesting tool to study the evolution and propagation of seismic waves. It will gain further importance with increasing computational capabilities. Nevertheless, modeling always depends on input in form of parameters and boundary conditions that can only be provided by field and laboratory experiments. We believe that putting the pieces together will make the difference in improving our understanding of seismic signals that emerge from an active volcano.

6 Acknowledgments

We kindly thank the people at the *Institut für physikalische Geodäsie* at the Technical University Darmstadt, Germany, for providing us with the digital elevation model of Mount Merapi. The calculations have been performed on the Hitachi SR8000 at the *Leibniz-Rechenzentrum* in Munich.

References

- Almendros, J., Chouet, B., Dawson, P., 2001a. Spatial extent of a hydrothermal system at Kilauea Volcano, Hawaii, determined from array analyses of shallow long-period seismicity, 1. Method. *J. Geophys. Res.* 106 (B7), 13565–13580.
- Almendros, J., Chouet, B., Dawson, P., 2001b. Spatial extent of a hydrothermal system at Kilauea Volcano, Hawaii, determined from array analyses of shallow long-period seismicity, 2. Results. *J. Geophys. Res.* 106 (B7), 13581–13597.
- Benites, R., Aki, K., 1994. Ground motion at mountains and sedimentary basins with vertical seismic velocity gradient. *Geophys. J. Int.* 116, 95–118.
- Bouchon, M., Schultz, C. A., Toksöz, M. N., 1996. Effect of three-dimensional topography on seismic motion. *J. Geophys. Res.* 101 (B3), 5835–5846.
- Clayton, R., Engquist, B., 1977. Absorbing boundary conditions for acoustic and elastic wave equations. *Bull. Seism. Soc. Am.* 67, 1529–1540.
- Frankel, A., Leith, W., 1992. Evaluation of topographic effects on P and S-waves of explosions at the northern Novaya Zemlya test site using 3-D numerical simulations. *Geophys. Res. Lett.* 19 (18), 1887–1890.
- Fuyuki, M., Matsumoto, Y., 1980. Finite difference analysis of Rayleigh wave scattering at a trench. *Bull. Seism. Soc. Am.* 70 (6), 2051–2069.
- Graves, R. W., 1996. Simulating seismic wave propagation in 3D elastic media using staggered-grid finite differences. *Bull. Seism. Soc. Am.* 86 (4), 1091–1106.
- Hestholm, S., 1999. Three-dimensional finite difference viscoelastic wave modelling including surface topography. *Geophys. J. Int.* 139, 852–878.
- Jih, R.-S., McLaughlin, K. L., Der, Z. A., 1988. Free-boundary conditions of arbitrary polygonal topography in a two-dimensional explicit elastic finite-difference scheme. *Geophysics* 53 (8), 1045–1055.
- Kawase, H., 1988. Time-domain response of a semi-circular canyon for incident SV, P and Rayleigh waves calculated by the discrete wavenumber boundary element method. *Bull. Seism. Soc. Am.* 78, 1415–1437.
- Luzón, F., Sánchez-Sesma, F. J., Rodríguez-Zúñiga, J. L., Posadas, A. M., García, J. M., Martín, J., Romacho, M. D., Navarro, M., 1997. Diffraction of P, S and Rayleigh waves by three-dimensional topographies. *Geophys. J. Int.* 129, 571–578.
- Moczo, P., Bystrický, E., Kristek, J., Carcione, J. M., Bouchon, M., 1997. Hybrid modeling of P-SV seismic motion at inhomogeneous viscoelastic topographic structures. *Bull. Seism. Soc. Am.* 87 (5), 1305–1323.
- Neuberg, J., Pointer, T., 2000. Effects of volcano topography on seismic broadband waveforms. *Geophys. J. Int.* 143, 239–248.
- Ohminato, T., Chouet, B. A., 1997. A free-surface boundary condition for including 3D topography in the finite-difference method. *Bull. Seism. Soc. Am.* 87 (2), 494–515.
- Pitarka, A., Irikura, K., 1996. Modeling 3D surface topography by finite-

- difference method: Kobe-JMA station site, Japan, case study. *Geophys. Res. Lett.* 23 (20), 2729–2732.
- Ripperger, J., 2001. Volcano topography in 3-D seismic wave simulation, Diploma thesis, Ludwig-Maximilians-University, Munich, (unpublished).
- Robertsson, J. O. A., Holliger, K., 1997. Modeling of seismic wave propagation near the earth's surface. *Phys. Earth planet. Inter.* 104, 193–211.
- Ruud, B., Hestholm, S., 2001. 2D surface topography boundary conditions in seismic wave modelling. *Geophys. Prospect.* 49, 445–460.
- Sánchez-Sesma, F. J., Campillo, M., 1991. Diffraction of P, SV and Rayleigh waves by topographic features: A boundary integral formulation. *Bull. Seism. Soc. Am.* 81 (6), 2234–2253.
- Tessmer, E., Kosloff, D., 1994. 3-D elastic modeling with surface topography by a Chebychev spectral method. *Geophysics* 59 (3), 464–473.
- Tessmer, E., Kosloff, D., Behle, A., 1992. Elastic wave propagation simulation in the presence of surface topography. *Geophys. J. Int.* 108, 621–632.
- Virieux, J., 1986. P-SV wave propagation in heterogeneous media: Velocity-stress finite-difference method. *Geophysics* 51 (4), 889–901.
- Wassermann, J., Ohrnberger, M., 2001. Automatic hypocenter determination of volcano induced seismic transients based on wavefield coherence - an application to the 1998 eruption of Mt. Merapi, Indonesia. *J. Volcanol. Geotherm. Res* 110, 57–77.

Table 1

Parameters of the simulation run

P-wave velocity v_p	2800 $\frac{m}{s}$
S-wave velocity v_s	1500 $\frac{m}{s}$
Density ρ	2500 $\frac{kg}{m^3}$
Model size $nx \times ny \times nz$	500 x 500 x 350
Width of damping region	50 grid points
Grid spacing $dx = dy = dz$	15 m
Total seismogram length t	8 s
Time-step dt	0.00262 s
Number of time steps nt	3049
Dominant source frequency f_0	2 Hz
Grid points / wavelength	25

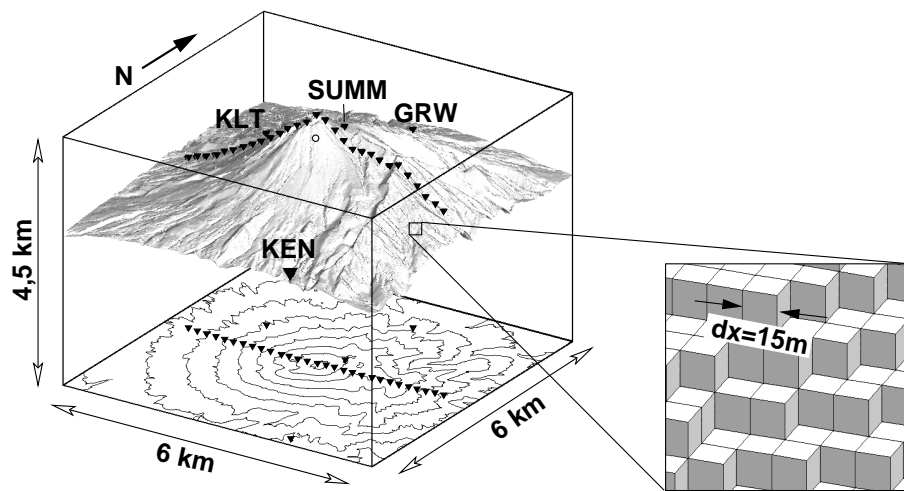


Fig. 1. Sketch of the model setup. Black triangles mark receiver positions and the open circle represents the source. In the FD method we use, the topography is discretized in a staircase shape as displayed in the inset. To avoid artefacts from this representation a very fine grid spacing of 15m is used. The inner part of the model is shown without the damping region around it.

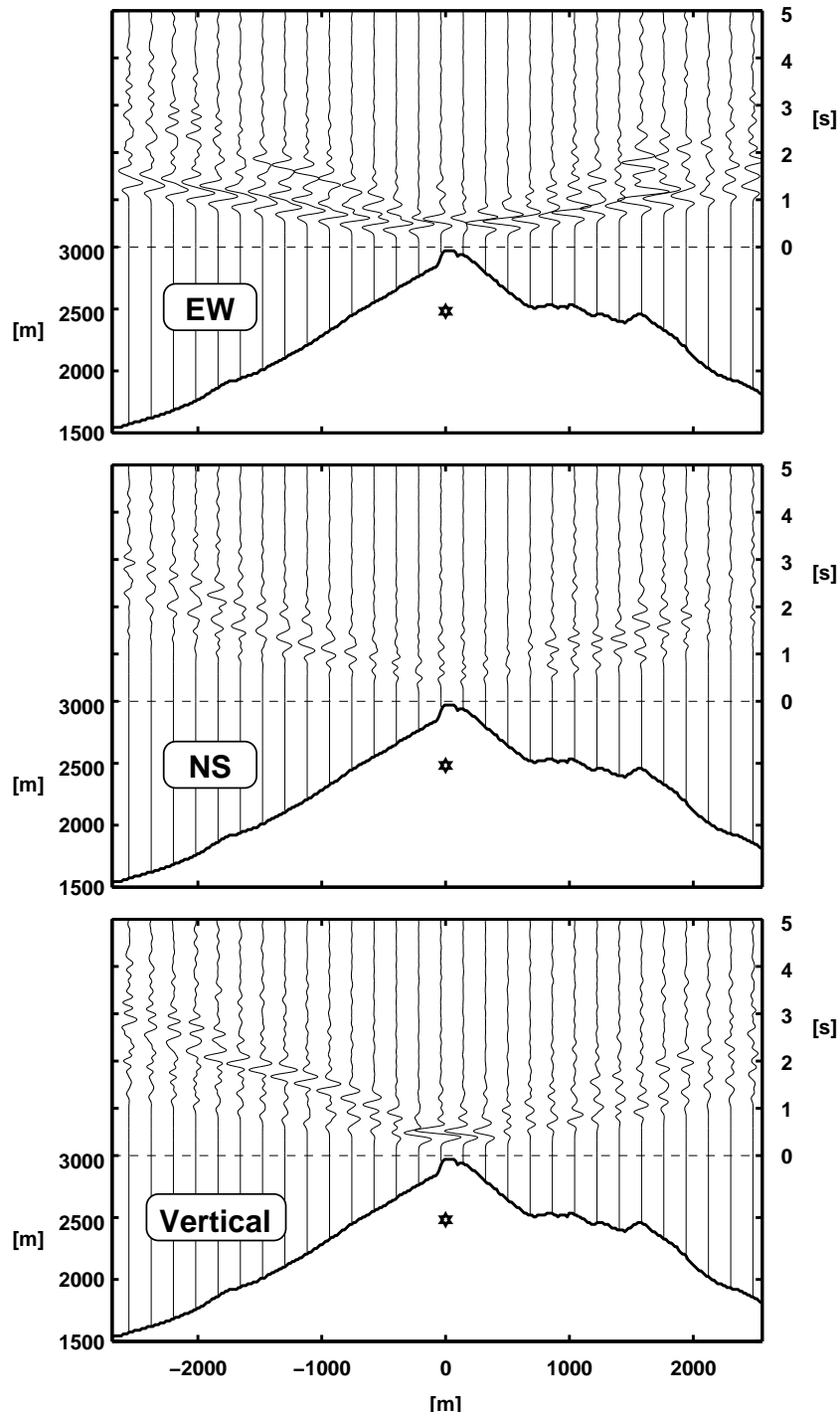


Fig. 2. Synthetic seismograms calculated for receivers along a EW-profile across the summit. Horizontal dashed line indicates the starting time of the simulation. All traces are scaled with the hypocentral distance to account for geometrical spreading. Note the amplification for the receiver on top of the small ridge on the eastern flank, especially on the EW-component.

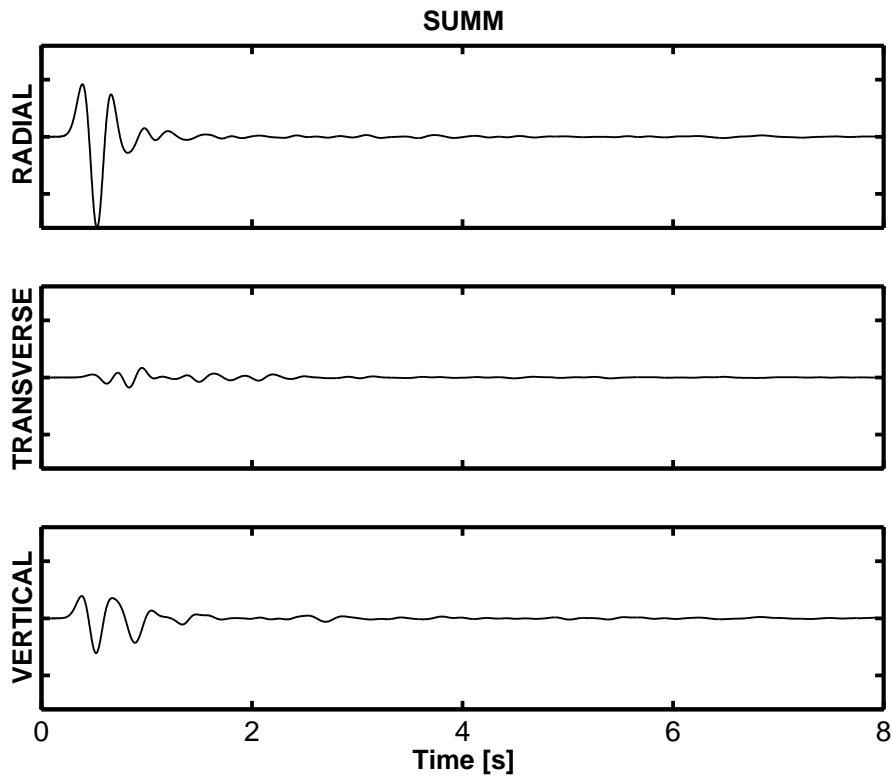


Fig. 3. *Synthetic velocity seismograms calculated for the site of the array SUMM. Since this site is located very close to the source, most of the energy is concentrated in the very first part of the seismograms.*

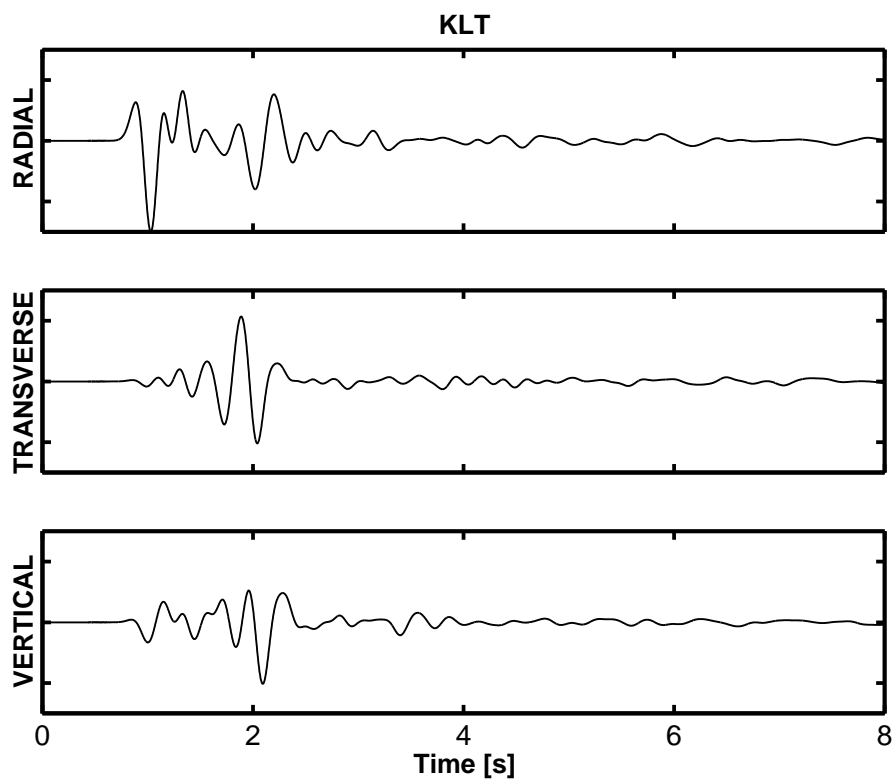


Fig. 4. Synthetic velocity seismograms calculated for the site of the array KLT. All traces are normalized to the maximum of all three components of this receiver. Note the comparably high amplitudes on the transverse component.

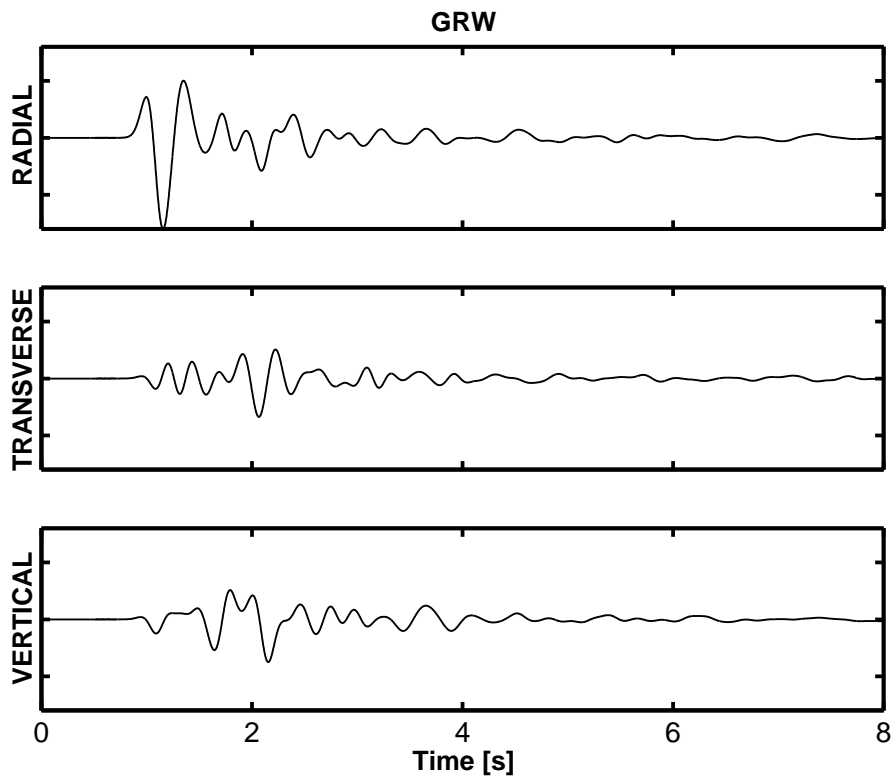


Fig. 5. *Synthetic velocity seismograms calculated for the site of the array GRW. All traces are normalized to the maximum of all three components of this receiver.*

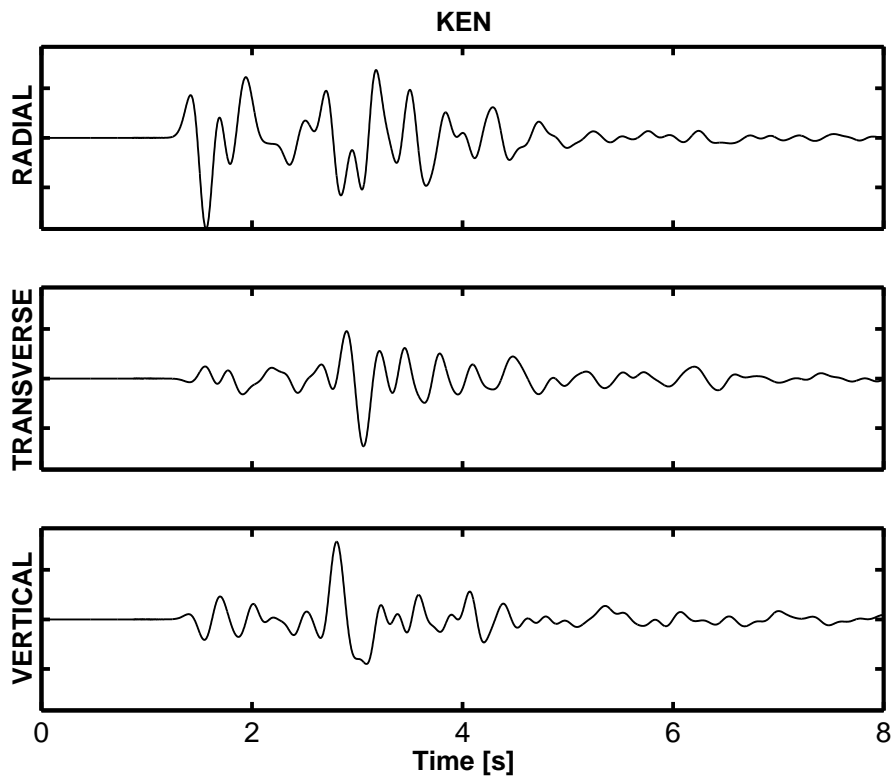


Fig. 6. *Synthetic velocity seismograms calculated for the site of the array KEN. All traces are normalized to the maximum of all three components of this receiver.*

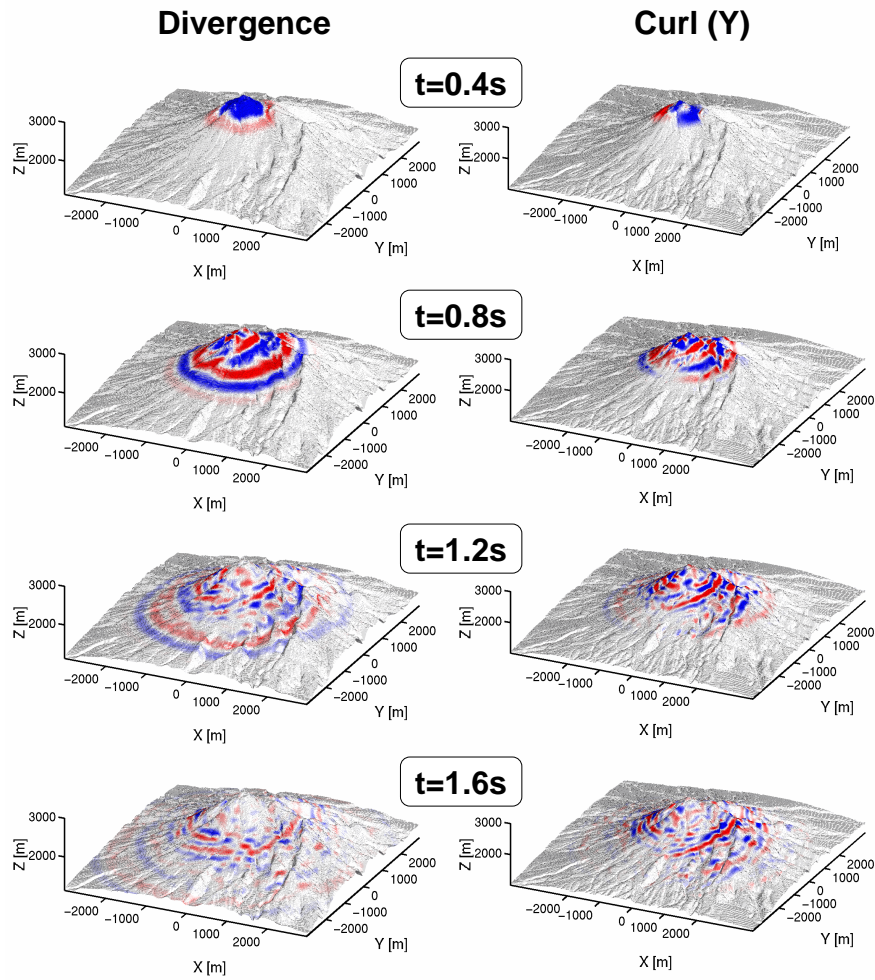


Fig. 7. Snapshots of wave propagation at the free surface. The divergence and the y -component of the curl of the velocity field are shown at different time steps. Red and blue colors mark positive and negative values, respectively.

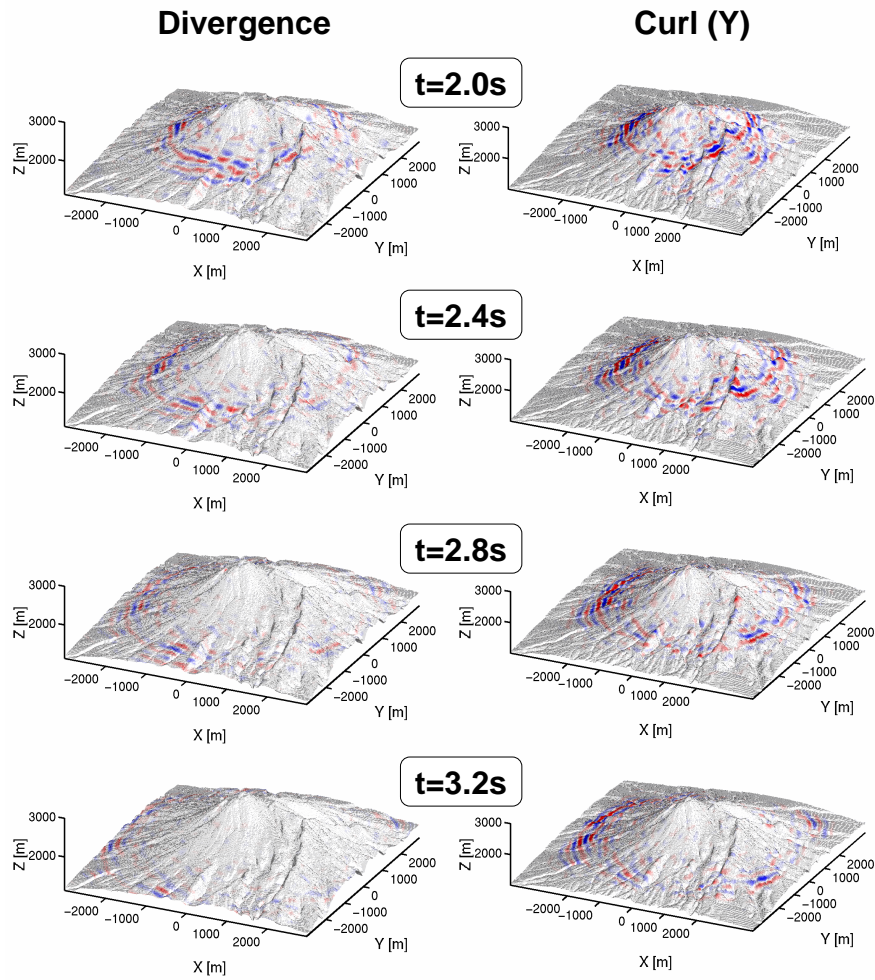


Fig. 8. Snapshots of wave propagation at the free surface. The divergence and the y -component of the curl of the velocity field are shown at different time steps. Red and blue colors mark positive and negative values, respectively.

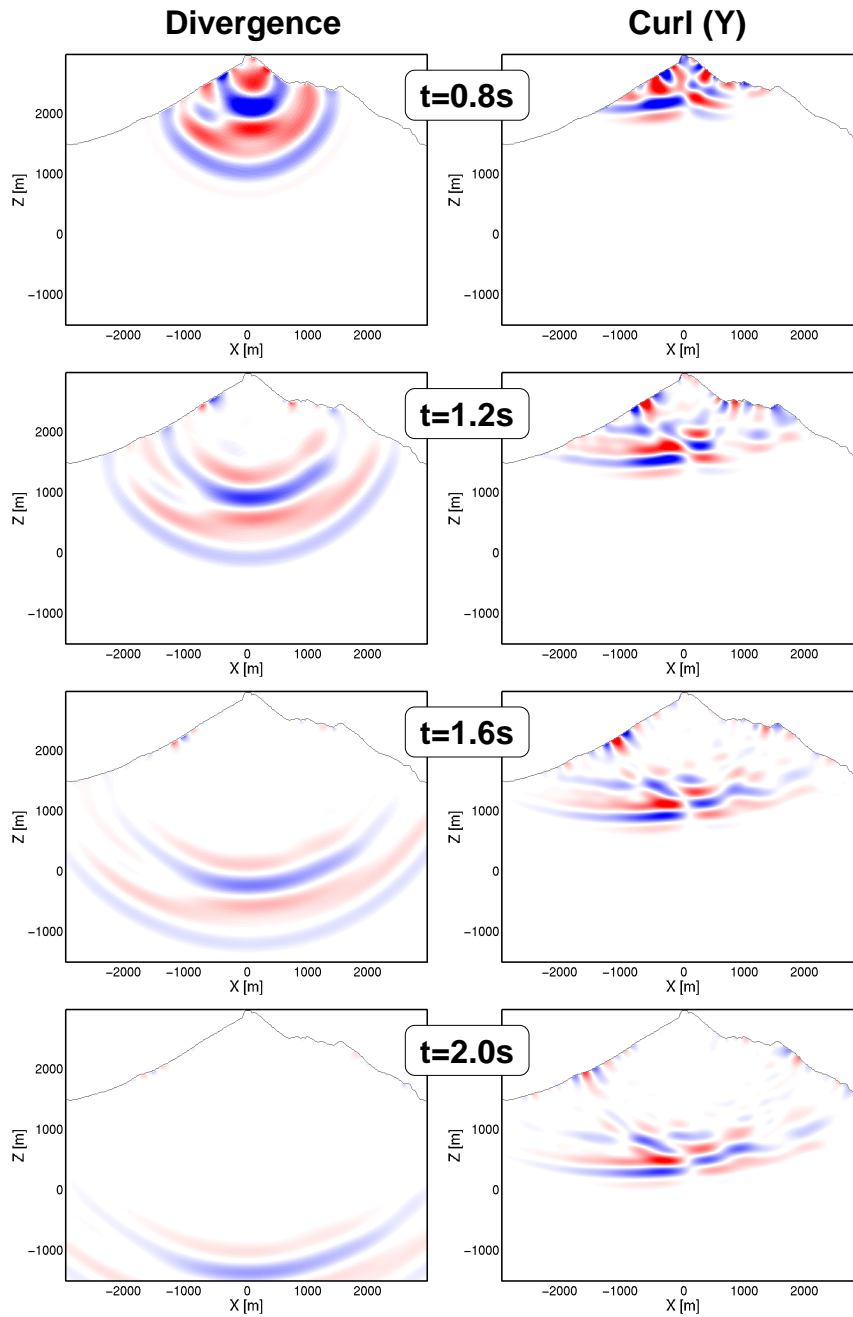


Fig. 9. Snapshots illustrating wave propagation for a vertical cross section below the receiver profile. The divergence and the y -component of the curl of the velocity field are shown at different time steps. Red and blue colors mark positive and negative values, respectively.

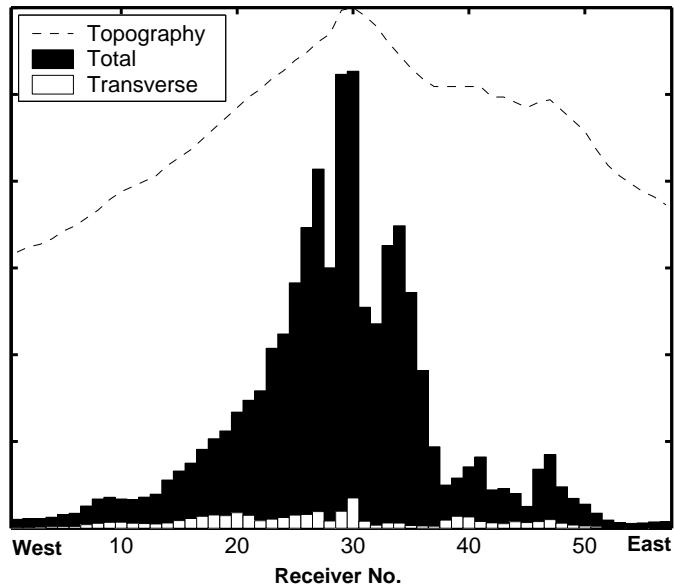


Fig. 10. *Seismic energy recorded along the profile. The sum of the squared amplitudes of all three components as a representation of the total energy (black) is displayed in comparison with the sum of the squared amplitudes of the transverse component (white) for each receiver. Axes are scaled in arbitrary units as only a qualitative effect is to be demonstrated. The dashed line sketches the topography along the profile. Note the difference between the smooth decay of the total energy on the western flank and the larger jumps and multiple peaks on the eastern side. The two peaks on the right coincide with topographic structures.*

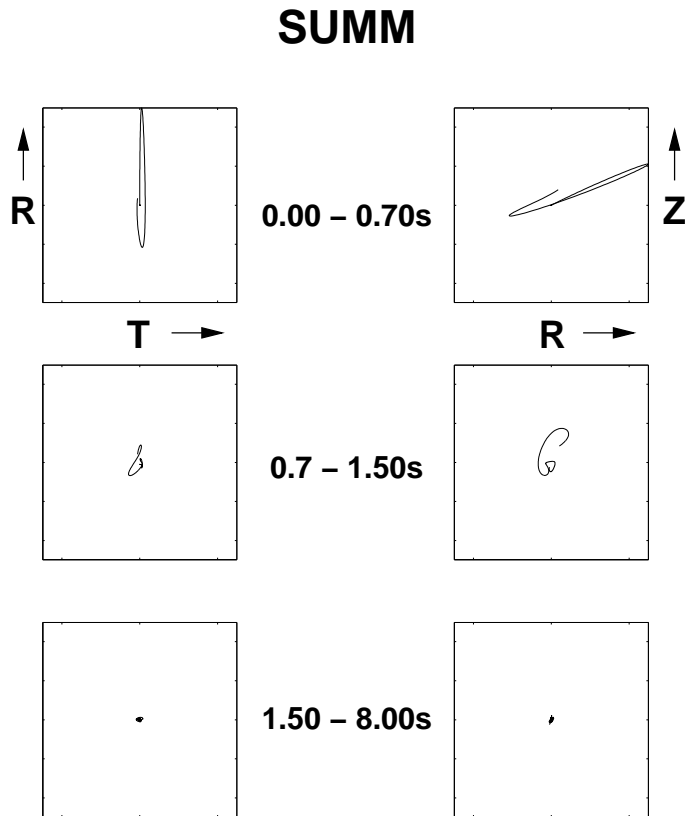


Fig. 11. Particle motion at the site of the array *SUMM* split into subsequent time intervals. Amplitudes are given in arbitrary units, normalized to the maximum of this receiver.

GRW

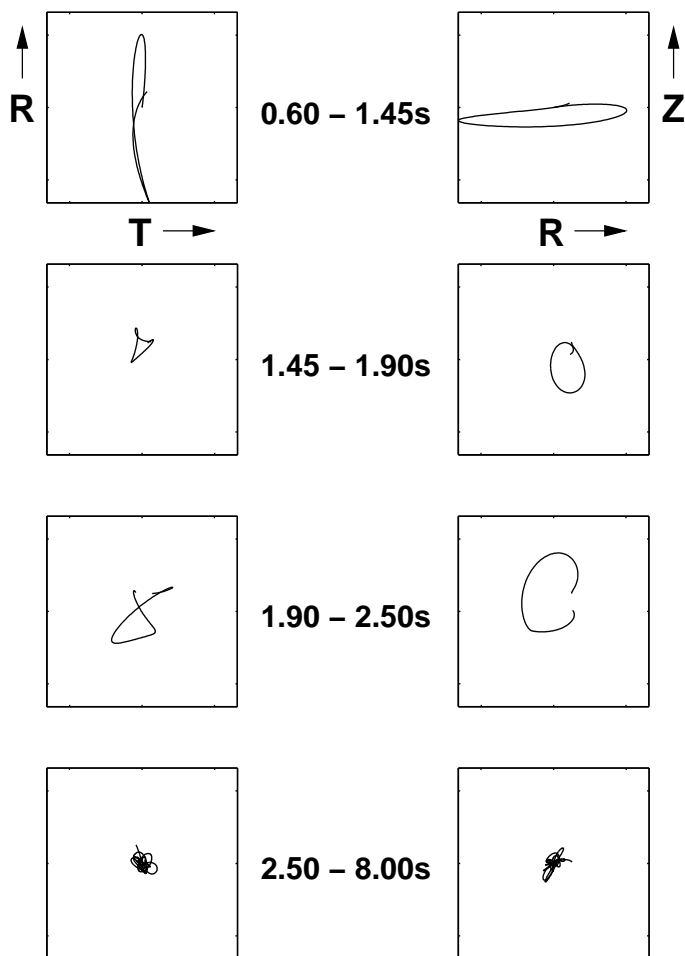


Fig. 12. Particle motion at the site of the sub-array GRW split into subsequent time intervals. Amplitudes are given in arbitrary units, normalized to the maximum of this receiver.

KLT

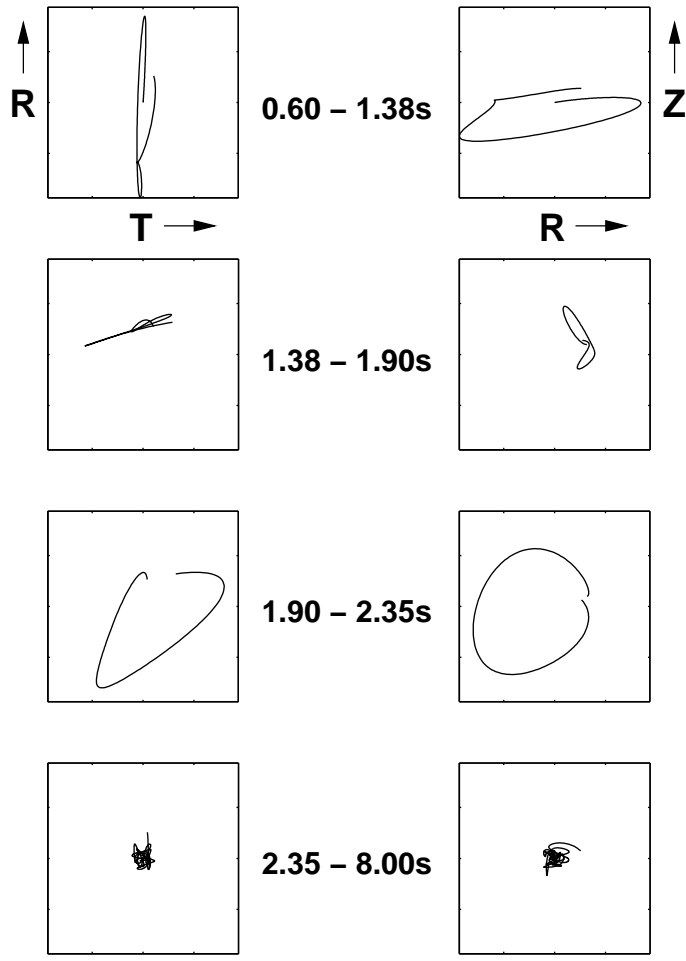


Fig. 13. Particle motion at the site of the sub-array KLT split into subsequent time intervals. Amplitudes are given in arbitrary units, normalized to the maximum of this receiver.

KEN

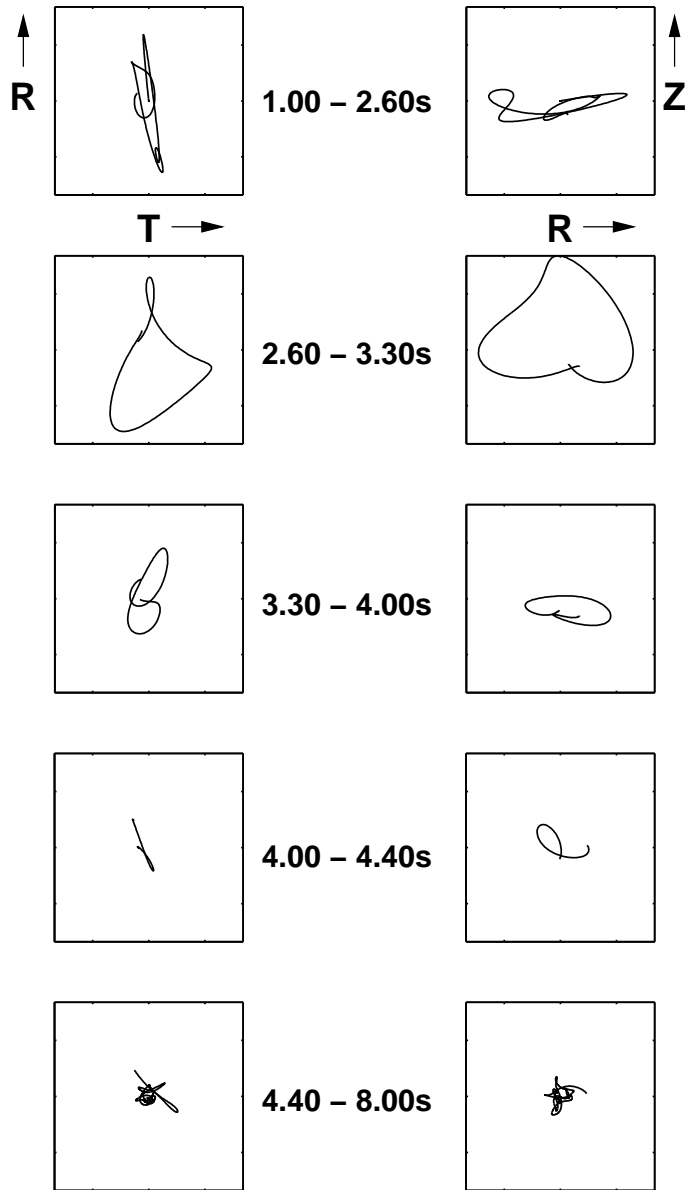


Fig. 14. Particle motion at the site of the sub-array *KEN* split into subsequent time intervals. Amplitudes are given in arbitrary units, normalized to the maximum of this receiver.

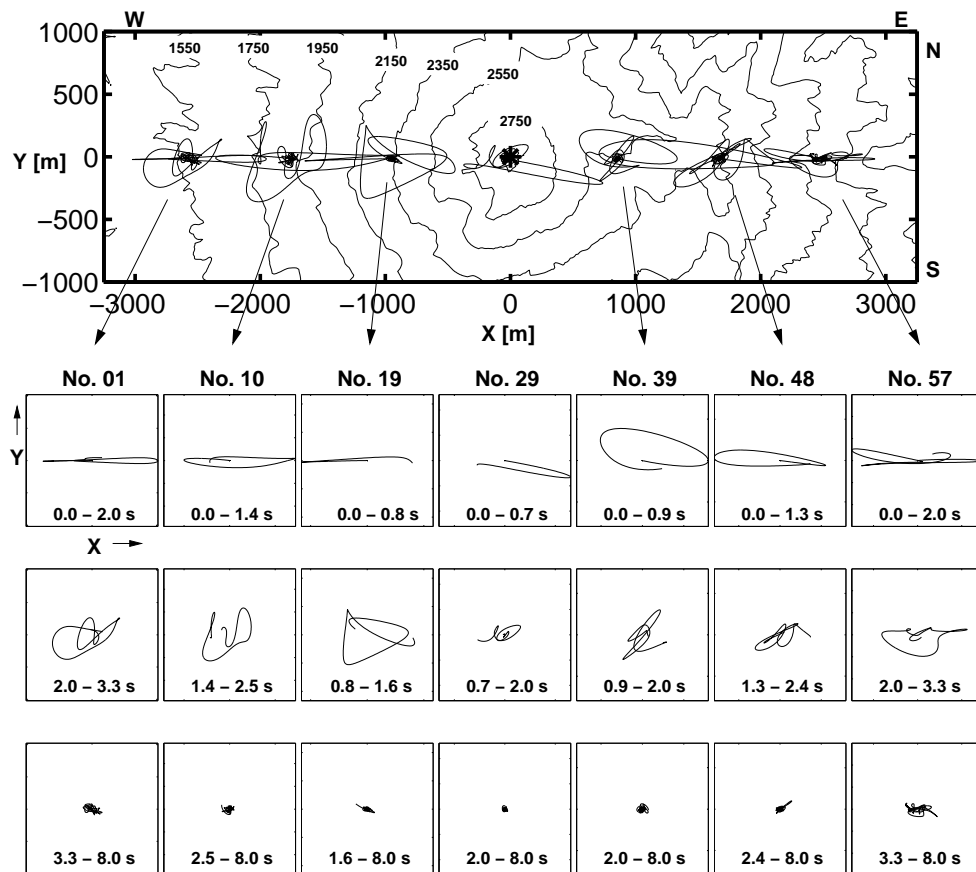


Fig. 15. Particle trajectories for selected receivers along the profile, projected into the horizontal plane. Amplitudes of the particle motion are given in arbitrary units. In the top sketch the amplitudes are scaled with the hypocentral distance of each receiver and for the three subsequent time segments the amplitudes are normalized with respect to the maximum of the receiver.

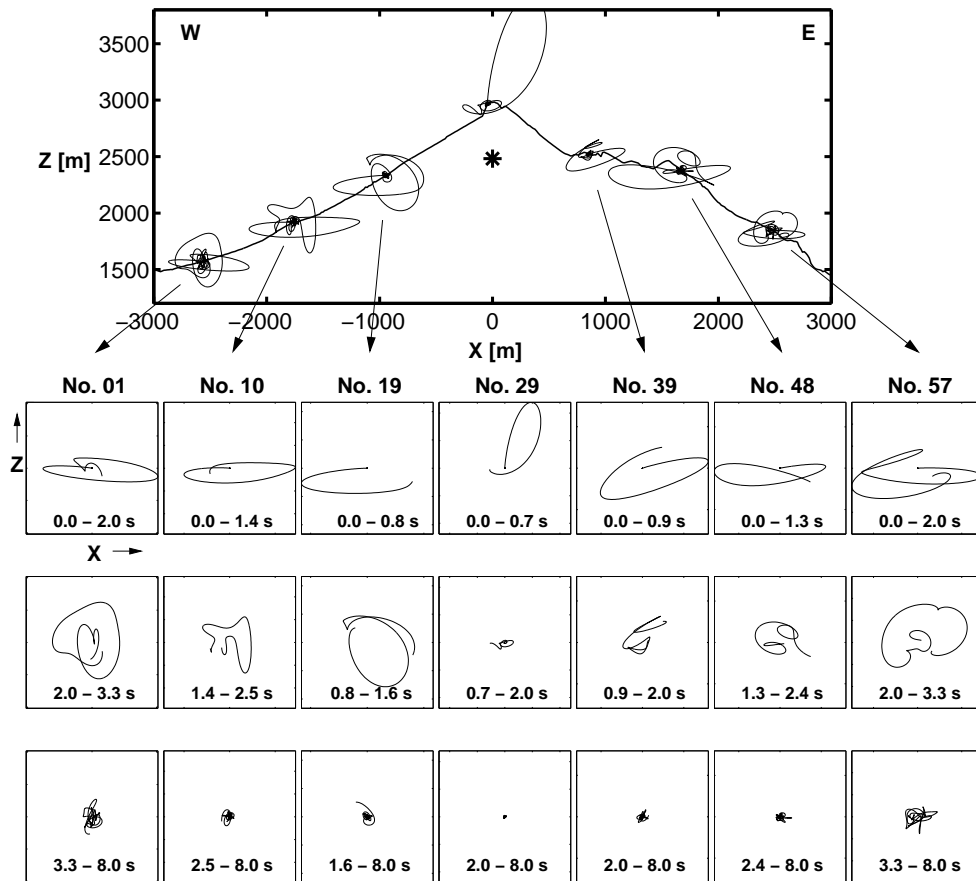


Fig. 16. Particle trajectories for selected receivers along the profile, projected into the vertical plane containing both receiver and source. Amplitudes of the particle motion are given in arbitrary units. In the top sketch the amplitudes are scaled with the hypocentral distance of each receiver and for the three subsequent time segments the amplitudes are normalized with respect to the maximum of the receiver.